

Wear mechanism and tribological characteristics of porous NiTi shape memory alloy for bone scaffold

Shuilin Wu,^{1,2} Xiangmei Liu,^{1,2} Guosong Wu,¹ Kelvin W. K. Yeung,³ Dong Zheng,⁴ C. Y. Chung,¹ Z. S. Xu,² Paul K. Chu¹

¹Department of Physics & Materials Science, City University of Hong Kong, Tat Chee Avenue, Kowloon, Hong Kong, People's Republic of China

²Hubei Province Key Laboratory for Industrial Biotechnology, Ministry-of-Education Key Laboratory for the Green Preparation and Application of Functional Materials, Faculty of Materials Science and Engineering, Hubei University, Wuhan, People's Republic of China

³Division of Spine Surgery, Department of Orthopaedics and Traumatology, The University of Hong Kong, Pokfulam, Hong Kong, People's Republic of China

⁴Union Hospital, Tongji Medical College, Huazhong University of Science and Technology, Wuhan, People's Republic of China

Received 13 October 2012; revised 7 December 2012; accepted 13 December 2012

Published online 11 February 2013 in Wiley Online Library (wileyonlinelibrary.com). DOI: 10.1002/jbm.a.34568

Abstract: The abraded debris might cause osteocytic osteolysis on the interface between implants and bone tissues, thus inducing the subsequent mobilization of implants gradually and finally resulting in the failure of bone implants, which imposes restrictions on the applications of porous NiTi shape memory alloys (SMAs) scaffolds for bone tissue engineering. In this work, the effects of the annealing temperature, applied load, and porosity on the tribological behavior and wear resistance of three-dimensional porous NiTi SMA are investigated systematically. The porous structure and phase transformation during the exothermic process affect the tribological properties and wear mechanism significantly. In general, a larger porosity leads to better tribological resistance but sometimes,

SMAs with small porosity possess better wear resistance than ones with higher porosity during the initial sliding stage. It can be ascribed to the better superelasticity of the former at the test temperature. The porous NiTi phase during the exothermic reaction also plays an important role in the wear resistance. Generally, porous NiTi has smaller friction coefficients under high loads due to stress-induced superelasticity. The wear mechanism is discussed based on plastic deformation and microcrack propagation. © 2013 Wiley Periodicals, Inc. *J Biomed Mater Res Part A*: 101A: 2586–2601, 2013.

Key Words: tribological behavior, phase transformation, NiTi shape memory alloys, porous, bone scaffold

How to cite this article: Wu S, Liu X, Wu G, Yeung KWK, Zheng D, Chung CY, Xu ZS, Chu PK. 2013. Wear mechanism and tribological characteristics of porous NiTi shape memory alloy for bone scaffold. *J Biomed Mater Res Part A* 2013;101A:2586–2601.

INTRODUCTION

Metals, such as stainless steels and nickel–titanium (NiTi) shape memory alloys (SMAs), are used in many applications due to their good strength, ductility, and compatibility. However, in some applications, there are concerns with Young's moduli mismatch with host materials thereby preventing proper distribution of stress and causing premature failure.^{1,2} Porous NiTi SMAs have attracted considerable attention because of their unique characteristics. For instance, a porous structure not only reduces the Young's modulus^{3–7} but also improves implant fixation by allowing tissue ingrowth in biomedical engineering.^{8,9} An additional surface treatment with nonline-of-sight protocols can further

enhance the performance.^{10–15} In fact, it is well known that loosening is one of the main failure mechanisms and debris released from the porous materials can often lead to massive osteolysis and catastrophic failure.^{16,17} Hence, it is imperative to consider the tribological properties during the design stage, with reduction of wear debris being one of the primary goals.

The wear properties of dense NiTi SMAs have been extensively investigated in the last two decades.^{18–24} The alloys have better wear resistance than conventional metals including some steels, Ni- and Co-based alloys, and titanium^{25–27} because the tribological performance of the latter materials depends on the mechanical properties such as

Correspondence to: P. K. Chu; e-mail: paul.chu@cityu.edu.hk or S. Wu; e-mail: shuilin.wu@gmail.com

Contract grant sponsor: City University of Hong Kong Applied Research Grant (ARG); contract grant number: 9667038

Contract grant sponsor: National Natural Science Foundation of China; contract grant numbers: 50901032, 51101053, 81271715

Contract grant sponsor: Ministry of Education Specialized Research Foundation for Doctoral Program of Universities; contract grant number: 20094208120003

Contract grant sponsor: Wuhan ChenGuang Research Program; contract grant number: 201150431134

hardness and work hardening, whereas the wear resistance of NiTi SMAs is believed to be determined by the stress or temperature-induced superelastic behavior as well as martensitic plate reorientation.^{24,27–29} In fact, under higher loads, some materials with high hardness, such as Co45 and 38CoCrMoAl alloys, exhibit worse wear resistance than NiTi.²⁷ However, whether superelasticity solely enhances the wear resistance of NiTi is controversial. Recent research by Zhang and Farhat²⁵ indicates that the wear properties of NiTi are not affected by the austenite transformation temperature in the range monitored. Although the wear resistance of NiTi is much better than that of Ti or Ni, it may not arise from superelasticity but rather the lower E/H and higher elastic recovery ratio of TiNi.²⁵ Yan³⁰ attributes the high wear resistance of NiTi to the combined effects of the small Young's modulus, low transformation stress, large recoverable transformation strain, and high-plastic yield strength of the martensite phase. The effects of other factors such as small voids in the composites of TiC(N)/TiNi²² and surface coatings on NiTi on the wear properties have also been probed.³¹ Nonetheless, studies on the wear resistance of NiTi SMAs have hitherto only focused on dense materials and superelasticity. To our knowledge, there have been no studies on the tribological properties of porous NiTi SMAs. Our research group has investigated the fabrication,^{5,32} surface modification by nonline-of-sight techniques (i.e., plasma immersion ion implantation, air oxidation, and chemical solution treatment can reach the exposed area despite the complex surface topography),^{10,12,14,33,34} and corrosion behavior of porous NiTi scaffolds.³⁵ In the work reported here, we systematically evaluate the effects of porosity and phase transformation on the tribological performance and wear resistance of porous NiTi SMA and discuss the related mechanisms.

EXPERIMENTAL DETAILS

Porous NiTi preparation

The porous NiTi materials were prepared by capsule-free hot isostatic pressing (CF-HIP) using the ABB mini HIP unit under argon. Equiatomic titanium and nickel powders were used as the starting materials. Two different ratios of ammonium acid carbonate (NH_4HCO_3) powders were used as the foaming agent to produce two kinds of sintered porous NiTi scaffolds with final porosities of 18 vol % (A) and 36 vol % (B), respectively. The powders were thoroughly mixed in a horizontal universal ball mill and pressed into green compacts under a pressure of 200 MPa using a hydraulic machine before sintering by CF-HIP under argon. Details about the CF-HIP process including mixing, cold pressing, removal of the foaming agent before sintering, and foaming mechanism can be found in our previous publications.^{5,14} The sintered porous NiTi scaffolds were linearly cut into pieces 2 mm thick with a diameter of 12.7 mm. All the samples were mechanically polished by SiC water sandpaper progressively up to 2400 grit, ultrasonically rinsed with acetone and ethanol, and then oven-dried before further experiments. As-received dense NiTi SMAs (50.8 at % Ni and 49.2 at % Ti) with the same dimensions (designated as D) were tested for comparison.

Differential scanning calorimetry analysis

After CF-HIP, both the dense and porous NiTi SMAs were annealed at 200°C, 400°C, or 500°C in a tube furnace under a continuous flow of 99.995% high purity argon for 0.5 h under atmospheric conditions followed by quenching in ice water. The transformation behavior and characteristic temperature were determined by differential scanning calorimetry (DSC) thermal analysis (TA 2910 Instrument). The weight of the specimens was between 10 and 20 mg. In the DSC TA, the samples were heated to 100°C, kept isothermally for 2 min to establish thermal equilibrium, cooled down to -50°C , kept isothermally for another 2 min, and then heated to 100°C again. The heating and cooling rates were 5°C/min.

Tribological assessment

The wear test was performed on flat porous NiTi samples at room temperature (RT) under air atmosphere using a ball-on-disk wear tester (Model POD-2; TEER Coating). The wear apparatus was computer driven to create wear tracks to quantitatively determine the wear properties. It used a low speed/high torque motor to rotate a flat sample under a loaded wear ball. The balls used in the abrasive wear tests were standard WC-Co ones with a diameter of 5 mm. They created a circular wear track on the sample by offsetting the ball relative to the center of rotation of the sample. Under an applied load of 1 N, the balls scribed a 5 mm diameter wear trace on the sample surface as they rotated at a speed 200 rpm. The same procedures were repeated under applied loads of 2 and 3 N.

Surface characterization

The surface morphology of the porous NiTi materials was investigated using scanning electron microscopy (SEM JSM5200). The samples were examined under an optical microscopy (OM, OLYMPUS BH2-UMA) without rinsing to examine the real worn surface on the porous NiTi SMA. The phase composition of the porous NiTi fabricated by CF-HIP was determined on a Siemens D500 X-ray diffractometer equipped with a Cu $K\alpha$ X-ray source operated at 40 kV and 30 mA. X-ray photoelectron spectroscopy (XPS; (Physical electronics PHI 5802, Minnesota) was performed to determine the chemical composition of the surface. An aluminum X-ray source with a power of 350 W was used under a vacuum of 2×10^{-8} Pa and the analytical area was approximately 0.8 mm². The photoelectron take-off angle was 45°. Survey scans spanning a binding energy range of 0–1000 eV with a pass energy of 187.85 eV and 0.8 eV/step were first acquired to identify the elemental species. Based on the different thickness of the surface layer, an argon sputter rate of about 3 nm/min was adopted. The binding energies were calibrated by the C 1s peak at 284.6 eV and a Gaussian-Lorentzian peak fitting model was utilized to deconvolute the Ti 2p spectra.

The wear morphologies were examined by SEM (JSM5200 and JSM 820). The chemical compositions of wear debris were measured by energy dispersive spectroscopy (EDS).

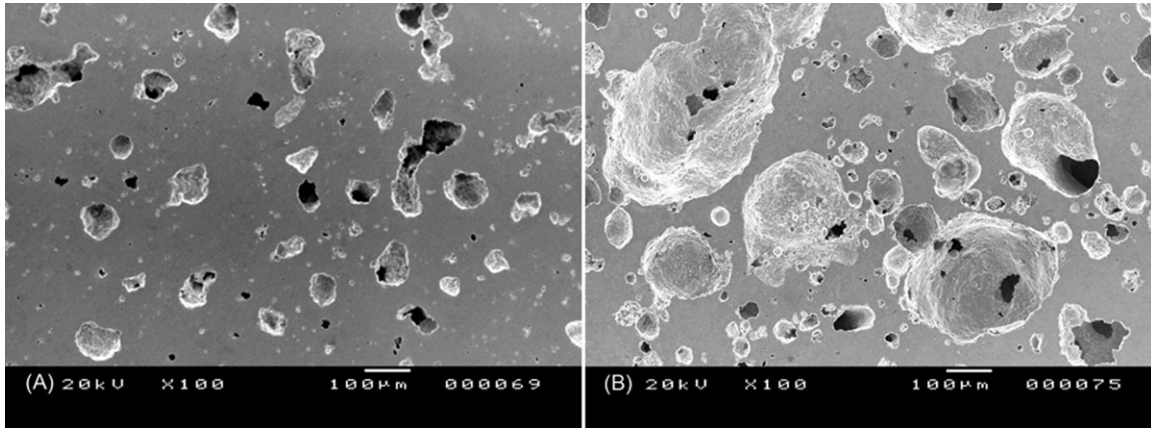


FIGURE 1. Surface morphologies of porous NiTi with different porosities: sample A 18 vol % and sample B 36 vol %.

Hardness measurements

The cross-sectional hardness from the top surface to the substrate was determined on a nanoindenter (MTS Nano Instruments XP) equipped with the continuous stiffness measurement capability and a Berkovich (three-sided pyramid) indenter. Before testing, the five sites were selected under OM and tests were subsequently going on automatically following the given program, and the average value was calculated.

RESULTS AND DISCUSSION

Microstructure and surface characterization

The porous structures of the CF-HIP sintered porous NiTi are depicted in Figure 1. The NiTi scaffold A with a low porosity of 18% possesses small pores in the range of 50–100 μm , whereas most of the pores in sample B having a porosity of 36 vol % are bigger (over 100 μm). As confirmed by previous results, a pore diameter of over 50 μm is proper for ingrowth of osteoblasts and surrounding tissues into the porous channels.^{36,37} Moreover, characteristics such as porosity and pore size can influence the phase transformation behavior³⁸ and impact the tribological characteristics of the scaffolds, and it needs to be demonstrated whether superelasticity which plays a crucial role in the wear resistance of dense NiTi SMAs^{27–29} has the same effects in porous NiTi SMAs. Therefore, it is necessary to determine the phase compositions of both dense NiTi and porous scaffolds sintered by CF-HIP. Figure 2 shows the phase compositions of the dense and porous NiTi samples determined by X-ray diffraction (XRD). As shown in Figure 2(a), the commercial dense SMA shows only the NiTi phase due to the homogeneous distribution of Ni and Ti during rapid fusion alloying as well as splat cooling. On the other hand, the CF-HIP sintered porous materials are composed of mainly NiTi phases of austenite B2 and martensite B19' with minor secondary phases such as Ni_4Ti_3 , Ni_3Ti , and NiTi_2 [Fig. 2(b)]. The occurrence of secondary phases is common in porous NiTi produced by powder metallurgical methods.^{39–43} According to the Ni–Ti binary diagram,⁴⁴ elemental Ni and Ti cannot be alloyed into the NiTi phase between 600 and 630°C but both Ni_3Ti and NiTi_2 can form in this temperature range. In

addition, starting at 630°C, NiTi_2 and Ni_3Ti can also form and be very stable below 984°C and 1118°C, respectively. Therefore, parameters such as the heating/cooling rates and temperature holding duration during CH-HIP can produce these secondary phases. The inhomogeneous distribution of

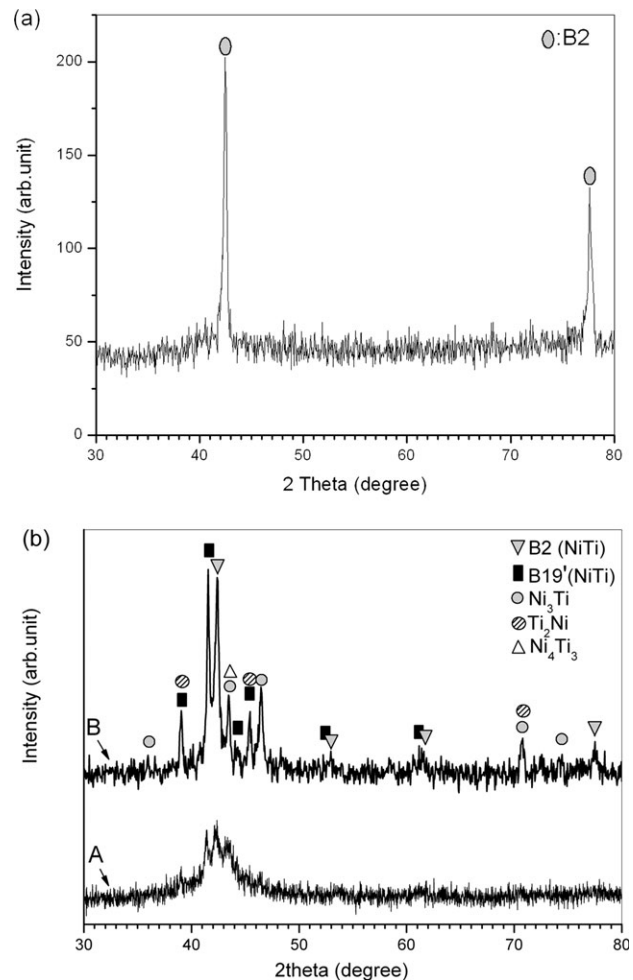


FIGURE 2. XRD patterns of NiTi SMAs: (a) dense sample and (b) porous samples as-sintered, B indicating 36% sample and A referring to 18% sample.

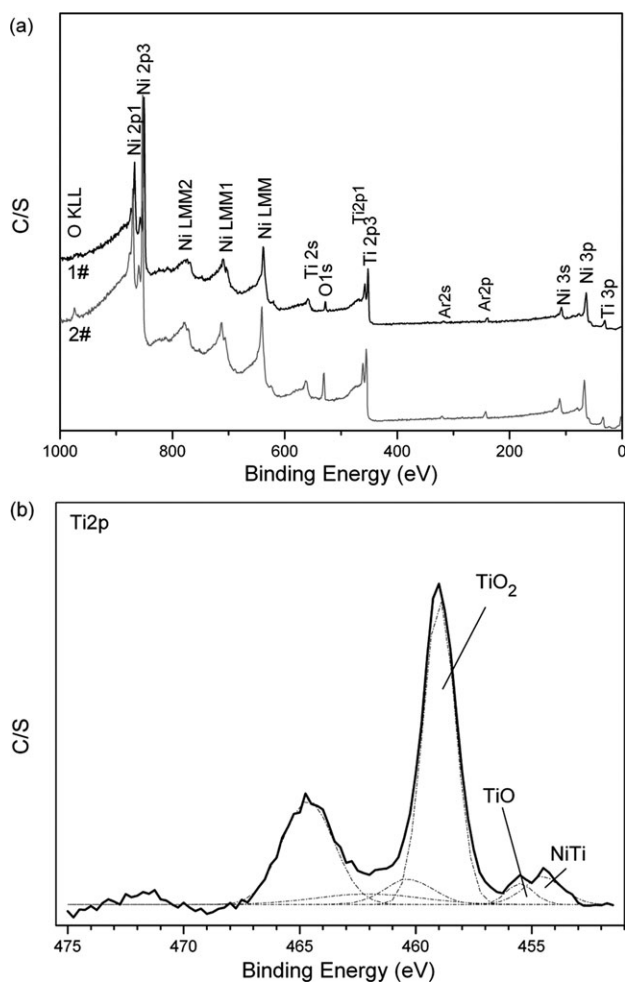


FIGURE 3. XPS spectra acquired from NiTi SMAs; (a) survey scan; 1# representing dense sample and 2# porous one; (b) Ti 2p fitted spectra of porous NiTi scaffold with the solid line (black color) indicating the experimental spectra and the dashed line (blue color) indicating the fitted spectra.

nickel and titanium in local areas is also responsible for the occurrence of secondary phases. For example, the NiTi₂ phase is formed when the Ti ratio is slightly higher than 50.5 at % whereas Ni₃Ti often forms when the Ti content is decreased as the temperature is increased, especially when the Ti content is below 43%. This elemental fluctuation usually arises from insufficient mixing or removal of the foaming agent. The minor intermetallic phase of Ni₄Ti₃ frequently forms during annealing or aging. It is well known that the superelasticity of NiTi SMAs is caused by temperature or stress-induced phase transformation between the two NiTi phases of martensite and austenite. In comparison, the dense materials exhibit a pure NiTi phase while a minor secondary phase impairs the superelastic behavior of porous SMAs, thus possibly influencing the tribological behavior of the porous NiTi alloys.

The chemical composition and distribution are also important as they influence the wear resistance. For example, microarc-induced Al₂O₃ enhances the wear resistance of NiTi SMAs appreciably.³¹ The XPS survey in Figure 3(a)

indicates the existence of oxygen on the surface of both dense and porous NiTi SMAs. The signal acquired from the porous sample (curve #2) is higher than that from the dense materials (curve #1). The high-resolution XPS spectra and fitted Ti 2p peak confirm that a thin layer of titanium oxide forms on the surface of the porous NiTi due to natural oxidation and minor oxidation during high temperature CF-HIP albeit in an argon ambient.⁵ It has been shown that natural oxidation on dense NiTi is inevitable during exposure to air or mechanical polishing.^{20,45} The XPS depth profile in Figure 4 shows that the thickness of the surface titanium oxide layer on the dense alloy is about 10 nm, whereas it is nearly 40 nm on the porous sample. The remaining of foaming agent (NH₄HCO₃) can possibly influence the surface chemical composition. Before sintering, the foaming agents in green compacts are removed by 200°C preheating in argon atmosphere, and our previous XPS analysis did not detect the foaming agent and its by-products.⁵

DSC analysis

Effects of porosity on phase transformation. To determine the difference in the superelasticity among porous NiTi A, B, and dense NiTi, that is, effects of porosity on the martensitic

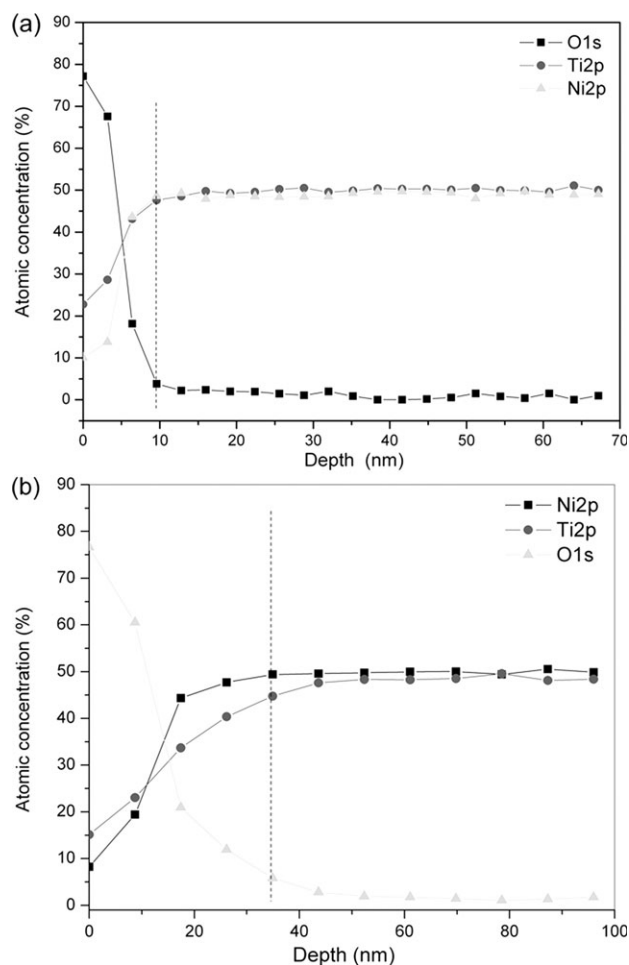


FIGURE 4. XPS depth profiles of NiTi samples: (a) dense and (b) porous.

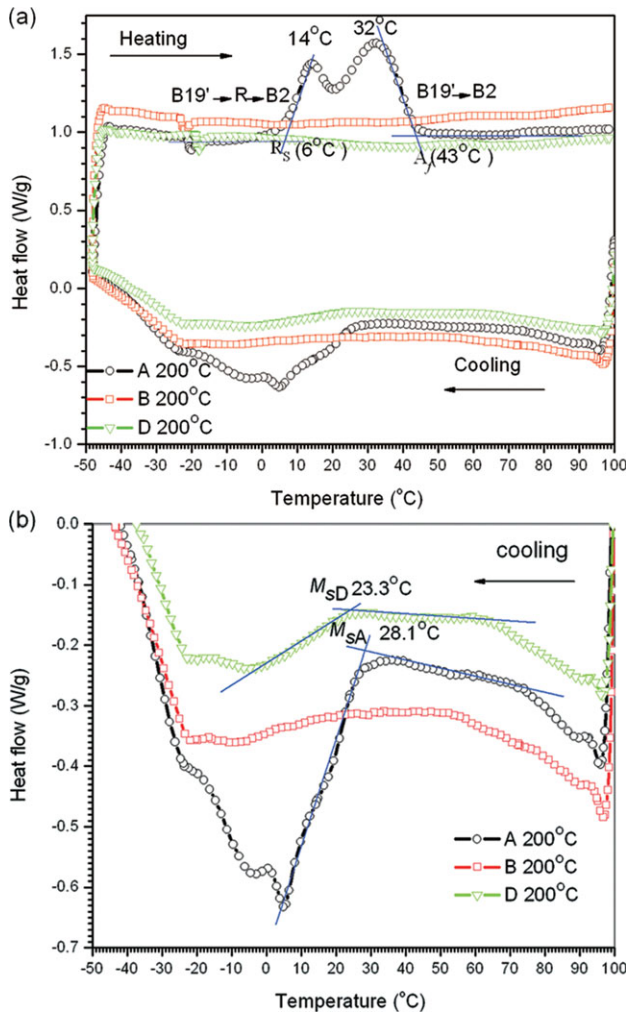


FIGURE 5. (a) DSC curves of porous samples A, B and dense sample D annealed at 200°C for 0.5 h; (b) magnified image of the exothermic reaction curve in (a). [Color figure can be viewed in the online issue, which is available at wileyonlinelibrary.com.]

transformation temperature, DSC is conducted to evaluate the starting and ending temperatures of the austenite, R-phase (an intermediate trigonal martensite), and martensite. They are designated as A_s , A_f , R_s , R_f , M_s , and M_f , respectively. As illustrated in Figure 5, sample A exhibits a clearly obvious multistep phase transformation (MSPT) during both the endothermic and exothermic processes, whereas samples B and D do not show clear phase transformation [Fig. 5(a)]. The magnified curve in Figure 5(b) indicates that the M_s starting temperature of samples A and D is about 28.1°C and 23.3°C during the exothermic process, respectively.

After annealing at 400°C, both the porous and dense NiTi SMAs show a clear MSPT behavior [Fig. 6(a)]. In the dense NiTi [Fig. 6(b)], the phase transformation comprises three parts. The first step is from B2 (austenite) to B19' (martensite) at a higher temperature. In this step, most B2 is converted into B19' and meanwhile, a small amount of B2 transforms into the R phase. The exothermic peaks at temperature below -10°C correspond to the phase transformation from a small trace of the R phase to B19'. Thus,

it can be concluded that M_s is about 47.1°C. In sample A, there is a small trace of phase transformation from B2 to R and subsequent R to B19' during the predominant process from B2 to B19' which proceeds in a wider temperature range between 33 and about -35°C. Hence, we believe that the corresponding M_s of sample A is about 33°C, although the bulk of the transformation occurs at about -4°C. However, there are two almost equal and independent courses in sample B. In the first stage, B2 begins to transform into the R phase at R_s of about 52.1°C and ends at R_f of about 26°C, and the second course from the R phase to B19' begins at M_s of about 0.5°C and ends at M_f of about -38°C.

Similar to the aforementioned phenomenon, after annealing at 500°C, all the samples exhibit MSPT during the exothermic process [Fig. 7(a)]. As shown in Figure 7(b), both samples D and B start transforming from the partial B2 to R phase at 38.1 and 36.2°C, but most of the B2 phase starts to transform into B19' at -7.4°C and 4.3°C, respectively. Therefore, in this case, the corresponding M_s should

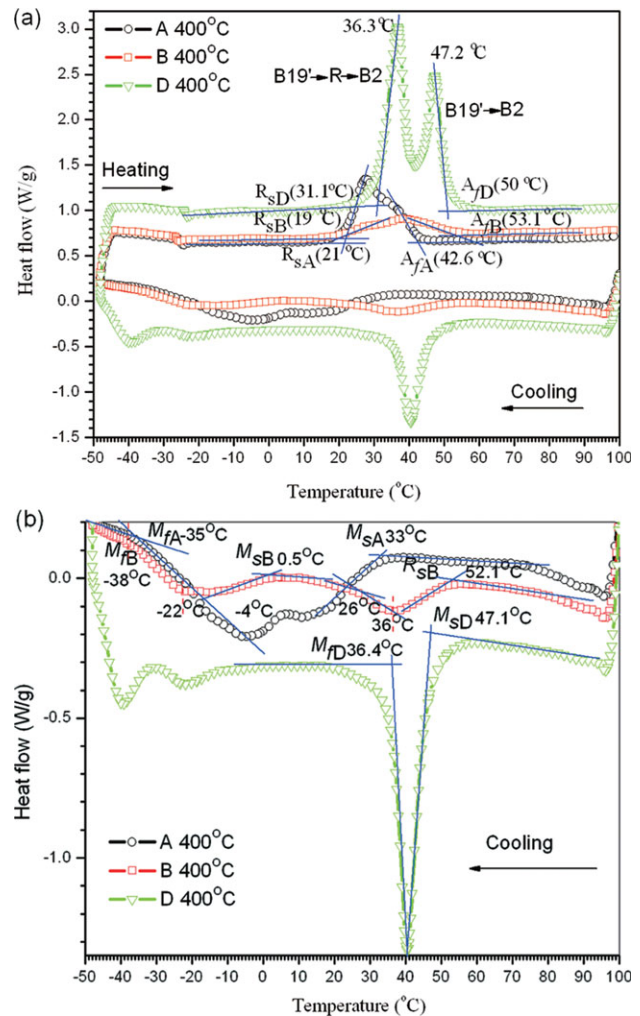


FIGURE 6. (a) DSC curves of porous samples A, B and dense sample D annealed at 400°C for 0.5 h; (b) magnified image of the exothermic reaction curve in (a). [Color figure can be viewed in the online issue, which is available at wileyonlinelibrary.com.]

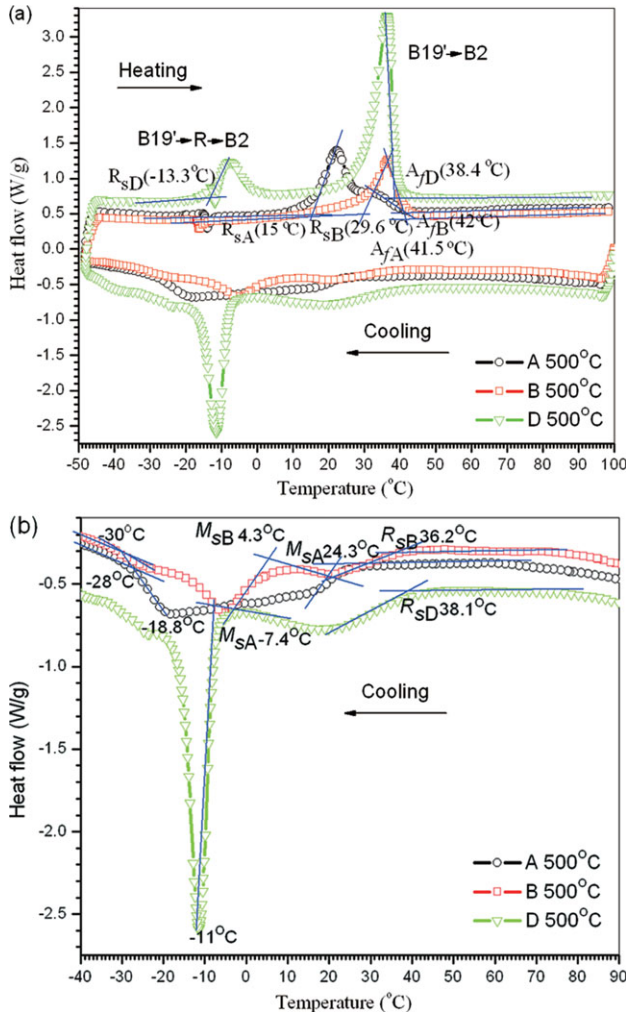


FIGURE 7. (a) DSC curves of porous samples A, B and dense sample D annealed at 500°C for 0.5 h; (b) magnified image of the exothermic reaction curve in (a). [Color figure can be viewed in the online issue, which is available at wileyonlinelibrary.com.]

be -7.4°C and 4.3°C for D and B, respectively. Although the M_s of sample A is about 24.3°C , it can be seen clearly from Figure 7(b) that the B19' transformation in this sample is much more gradual as the temperature is decreased, implying that the martensitic transformation in sample A is relatively difficult, that is, needing a larger driving force to complete the transformation. Consequently, compared with B and D, sample A appears to have lower superelasticity.

Effects of annealing temperature. As shown in Figure 8(a), the M_s of sample D shifts to a lower temperature when the annealing temperature is increased from 400°C to 500°C . In comparison with annealing at higher temperature, the 200°C annealed sample does not show obvious martensitic transformation during the exothermic process. According to Figure 8(b), the exothermic peak of sample A shifts to a lower temperature as the annealing temperature is increased, whereas the M_s temperature does not exhibit an obvious tendency. That is, 400°C annealing gives rise to the

highest M_s of 33°C but 500°C annealing leads to the lowest M_s of 24.3°C . However, the initial transformation from B2 to B19' or R phase becomes more gradual as the annealing temperature is raised, thus inducing the different phase portions between M_s and M_f during the exothermic process. As a consequence, the superelasticity and hardness are not only influenced by the M_s temperature, but also determined

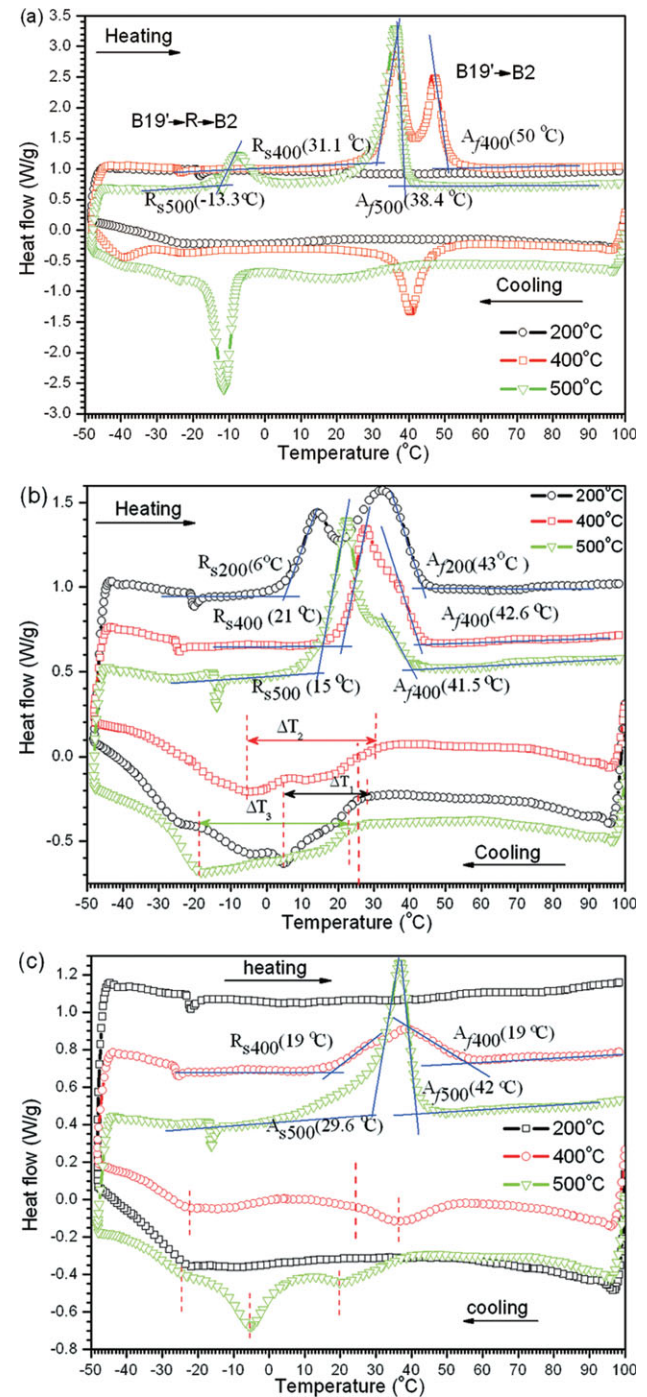


FIGURE 8. DSC curves of NiTi samples annealed at different temperature for 0.5 h: (a) sample D, (b) sample A, and (c) sample B. [Color figure can be viewed in the online issue, which is available at wileyonlinelibrary.com.]

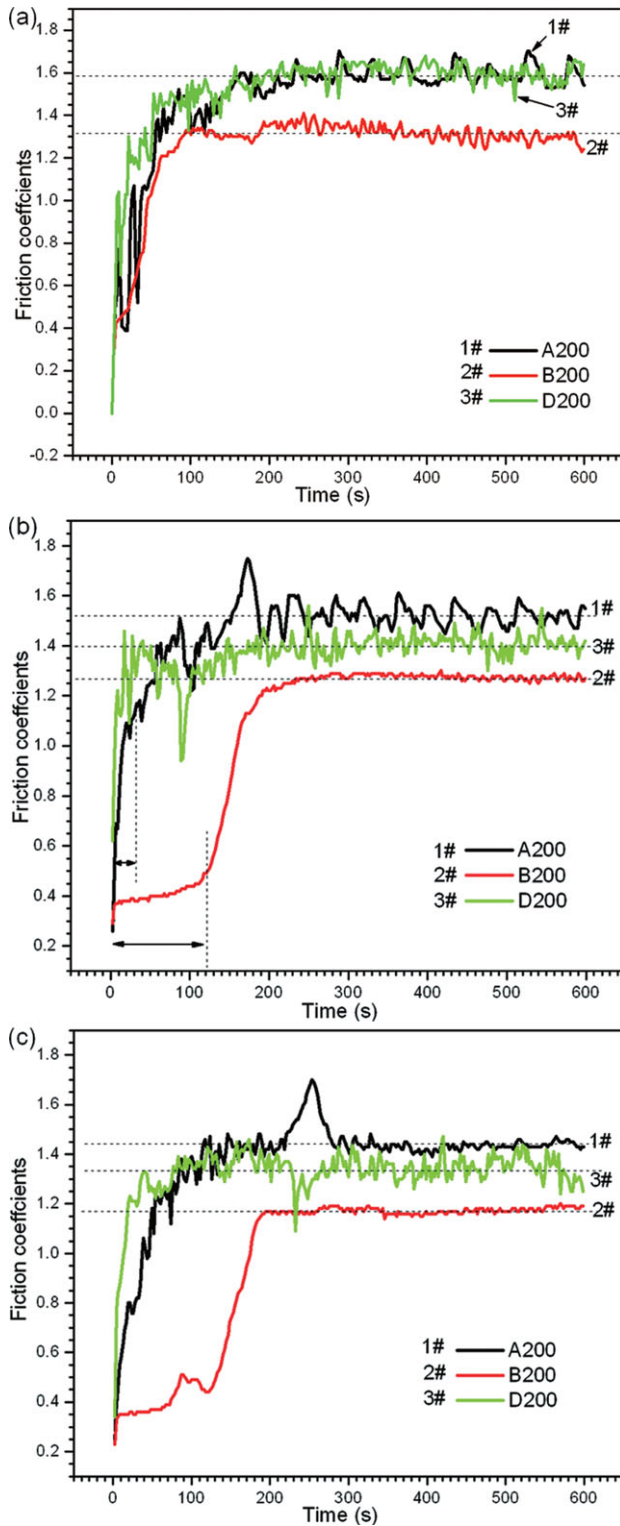


FIGURE 9. Evolution of friction coefficients with sliding time for the 200°C annealed samples A, B, and D under applied loads of (a) 1 N, (b) 2 N, and (c) 3 N. [Color figure can be viewed in the online issue, which is available at wileyonlinelibrary.com.]

by the phase proportion under the specific temperature. In sample B, which has a higher porosity, Figure 8(c) shows that the intensity of the dominant exothermic peak goes up

with increasing annealing temperature. The two equal exothermic peaks evolve into a three-step phase transformation when the annealing temperature is increased from 400°C to 500°C. The latter is composed of one dominant peak at -5°C related to the phase transformation from most B2 to B19', one shoulder peak at 20°C corresponding to the process of partial B2 to R phase, and the other one at -25°C correlated to the phase transformation from remaining R to B19'. In this case, besides M_s , both R_s and R_f can influence the hardness or superelasticity of the porous NiTi scaffold at a given temperature.

Tribological behavior

Friction coefficients. Figure 9 shows the evolution of the friction coefficients of the porous NiTi annealed at 200°C under different loads. Sample B with the highest porosity shows the lowest friction coefficient and best wear resistance among the three types of samples. Under dry wear conditions, the friction coefficients are determined by the shearing stress (S), nominal load (W), and apparent contact area (A) according to the following equation^{46,47}:

$$f = \frac{SA}{W} \quad (1)$$

Because a porous structure reduces the contact area, a higher porosity leads to a smaller contact area. In conventional materials, a higher porosity will yield lower friction coefficients, but an unexpected phenomenon is observed here. Sample A with 18% porosity shows a slightly higher value compared with sample D (dense NiTi), especially under loads of 2 and 3 N [Fig. 9(b,c)]. Therefore, besides the porosity (contact area), other factors must impact the tribological behavior. It has been shown that the superelasticity of NiTi SMAs can enhance the wear resistance.²⁷⁻²⁹ As shown in Figure 5(b), the M_s of sample A is 28.1°C, which is slightly higher than RT, whereas the value of sample D is 23.3°C that is slightly below RT. Hence, sample D should possess a complete austenite phase, whereas sample A has partially transformed martensite and austenite phases. It translates into higher hardness in sample D compared with sample A, which can be confirmed by the measurement of nanohardness. Figure 10 shows the evolution of hardness along the depth from the top surface. It can be observed that surface hardness of is higher than that of the inner side. The phenomena may be caused by the precipitation of more secondary phases on the outside. Because of the oxidation of NiTi alloy during the annealing process, one gradient Ni-rich layer forms along the depth, which induce the formation of Ni-rich secondary phases such as Ni_4Ti_3 and Ni_3Ti with a gradient distribution. The precipitation of these secondary phases along the grain boundary strengthens the substrate. There are more Ni-rich secondary phases on the outside than on the inner side, and consequently the surface hardness is higher than the inside. It is obvious that sample D has higher hardness than sample A in the range from top to about 460 nm depth. However, as the depth is increased, phase transformation from the remaining soft phase B19' to

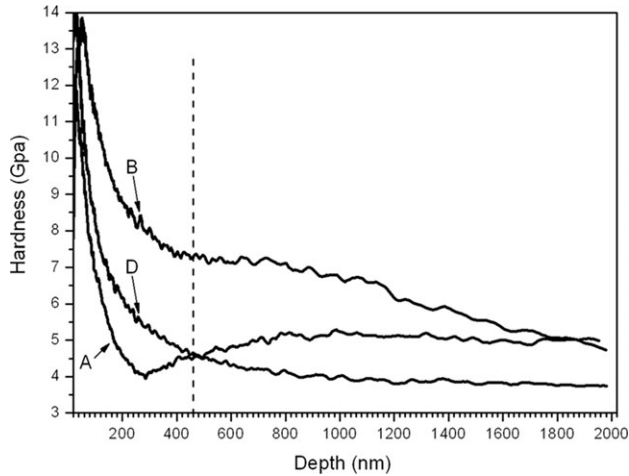


FIGURE 10. Hardness as a function of depth from the top surface for the 200°C annealed NiTi samples.

hard phase B2 occurs within the local area around the indenter. Thus, the hardness of sample A becomes higher than that of sample D below about 460 nm. In this course, interconnected porous structure could possibly induce the fluctuation of hardness. As shown in Figure 9, the friction coefficients decrease as the applied load is increased from 1 to 3 N for the three kinds of samples. It may be ascribed to stress-induced superelasticity during the wear test because a larger applied load can stimulate the superelasticity of NiTi SMAs more easily.

As shown in Figure 11, after annealing at 400°C, the porous NiTi materials generally exhibit much higher friction coefficients than dense SMAs. As shown in Figure 6(b), the M_s and M_f of sample D are 47.1°C and 36.4°C and much higher than RT. Hence, the main phase of sample D is monoclinic martensite during the wear test. With regard to sample B, the experimental temperature falls in the range between R_f (26°C) and M_s (0.5°C) and so the dominant one is the R phase of intermediate trigonal martensite in sample B at RT. In sample A, as shown in Figure 6(b), the exothermic reaction occurs within a wide range from 33°C to -35°C, and the main peak is located at -4°C. Hence, it can be concluded that sample A is composed of B2 together with R-phase and B19' at RT. Therefore, sample A possesses the highest hardness but sample D has the lowest hardness at RT. Figure 12 depicts the evolution of hardness along the depth profile for 400°C annealed samples. Sample A shows the highest value when depth is over about 300 nm away from the top. This is the reason why sample A has the lowest friction coefficients [Fig. 11(a,b)] but sample D exhibits the highest coefficient. According to the hardness curve in Figure 12, during the measurement of hardness by nanoindenter, the local phase transformation or work hardening possibly occurs for sample A, whereas it does not occur in samples B and D. This phenomenon can possibly be explained as following. When the phases around the indenter are composed of harder phase B2 and softer phase R or B19', like 200°C annealed sample A and 400°C annealed sample A, the energy caused by the pressure from the

indenter cannot be absorbed by the around harder phase B2, and thus induces the phase transformation from B19'/R to B2 or local work hardening. However, if it is the uniform single phase, the energy from the indenter could be absorbed by the around soft phase, and the work hardening and phase transformation could be avoided. Of course, the

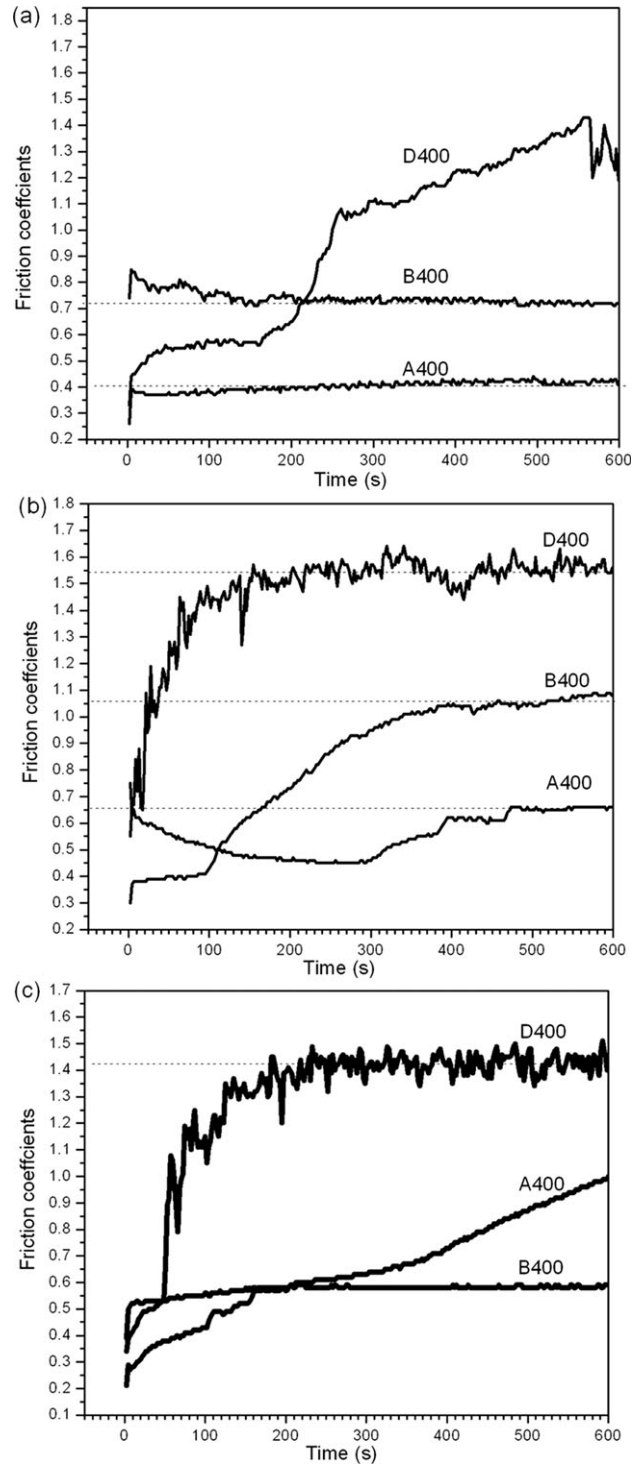


FIGURE 11. Evolution of friction coefficients for the 400°C annealed samples A, B, and D under applied loads of (a) 1 N, (b) 2 N, and (c) 3 N.

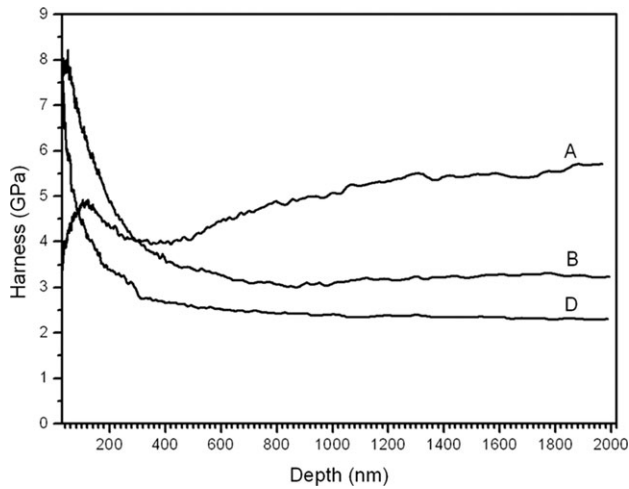


FIGURE 12. Hardness as a function of depth from the top surface for the 400°C annealed NiTi samples.

above deduction is based on the slowest loading speed and the tiny area around the nanoindenter. This phenomenon will be further investigated in the future. The surface conditions also play an important role in the tribological behavior. As shown in Figure 11(a), in the first wear stage from 1 to 200 s, sample D exhibits a stable zone with low friction coefficients at a load of 1 N due to the continuous titanium oxide film shown in Figures 3 and 4. In the initial stage, the continuous film can improve the wear resistance of the dense NiTi under a small applied load. However, the oxide film is easily destroyed as sliding proceeds, and so the friction coefficient goes up if the substrate is softer than the film. Because of the soft martensitic substrate in sample D, the friction coefficient increases after the thin oxide layer is destroyed. Under a large applied load, the oxide film is destroyed very quickly as shown in in Figure 11(b,c) for sample D. However, because of the porous structure, the surface oxide film is not continuous on the porous scaffolds. Therefore, in comparison with dense NiTi, this film has little effects on the friction coefficient of the porous samples. The other issue is the role of the porous structure. The porous materials can absorb some of the energy produced during the wear test thereby enhancing the tribological resistance. It is illustrated in Figure 11(b) that during the initial stage of about 100 s, sample B has smaller friction coefficients than sample A. As the sliding time is increased, the friction coefficient curves of the porous NiTi samples show fluctuating phenomena under loads of 2 and 3 N [Fig. 11(b,c)]. It is believed to be related to the stress-induced phase transformation in the surface layer of the NiTi alloys during the wear test, especially under larger applied loads.

As shown in Figure 13, similar to the phenomenon illustrated in Figure 11(a), the surface oxide film on sample D induces a region with stable and lower friction coefficients and as the applied load is increased, film damage is accelerated, as shown by the shorter flat ranges in Figure 13(a-c). Although sample D has the lowest M_s temperature of -5°C , it still has larger friction coefficients. It is very different from the results reported by Peña et al.¹⁸ that the wear

resistance of dense equiatomic NiTi alloys depends mainly on the M_s transformation temperature, which is related the hardness. The hardness shown in Figure 14 indicates that sample A has the highest hardness, whereas the sample D has the lowest value. It implies that in comparison with the

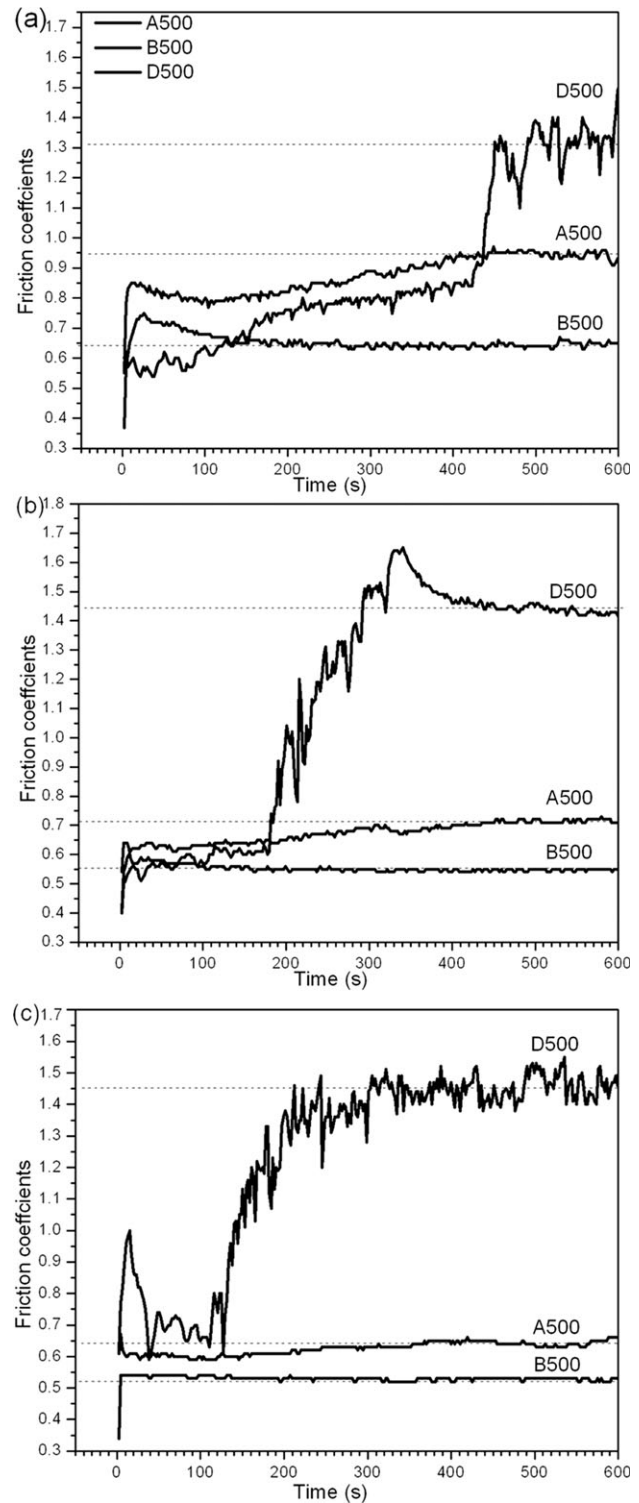


FIGURE 13. Evolution of friction coefficients for the 500°C annealed samples A, B, and D under applied loads of (a) 1 N, (b) 2 N, and (c) 3 N.

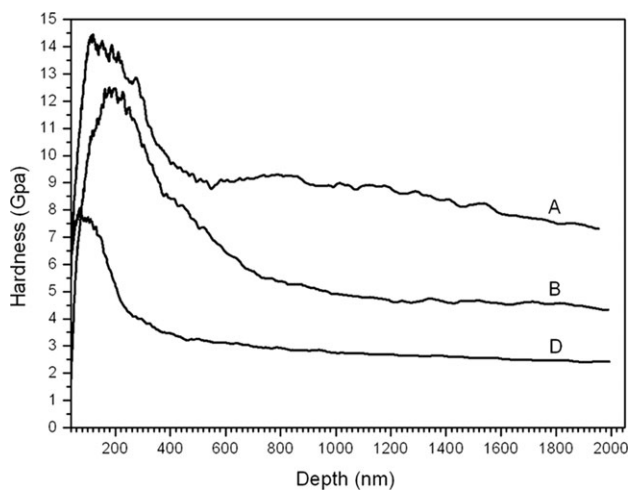


FIGURE 14. Hardness as a function of depth from the top surface for the 500°C annealed NiTi samples.

M_s temperature, other factor can also possibly influence the hardness of porous NiTi. For example, the annealing process maybe induces the precipitation of second phases that consolidate the substrate. In addition, the porous structure plays an important role in improving the wear resistance of the porous NiTi alloys. Sample B has smaller friction coefficients than sample A. Besides the higher porosity, the superelasticity impacts the wear resistance of the porous NiTi alloys. As shown in Figure 7, sample B has a lower M_s temperature than A. In addition, the phase transformation in sample A is more gradual than that in sample B as the temperature is decreased. It indicates that martensitic transformation in sample A is relatively difficult compared with that in the latter, because a larger driving force is required to complete the transformation. Hence, sample A has a smaller degree of superelasticity than sample B.

Figure 15 shows the effects of annealing temperature on the friction coefficients under a load of 3 N. In general, the friction coefficients of porous NiTi exhibit a decreasing tendency as the annealing temperature is increased. In sample A, although the DSC curve in Figure 8(b) shows that annealing at 200°C yields a lower M_s than 400°C, ΔT (temperature difference between M_s and the dominant peak temperature) of the former is much smaller than that of the latter. It suggests that the phase transformation in the former is quicker and thus, the former has a larger martensite portion than the latter. This leads to the lowest hardness and highest friction coefficients shown in Figure 15(a). Because the M_s temperature is below RT, annealing at 500°C results in the full austenite phase during the wear test and corresponding stable and lower friction coefficients. However, in comparison with annealing at 400°C, the exothermic curve of the sample annealed at 500°C shows a much larger ΔT [$\Delta T_3 > \Delta T_2$ as shown in Fig. 8(b)], indicating that the martensitic phase transformation is more difficult in the latter and better superelasticity in the former. It can be observed from Figure 15(a) that the former shows smaller friction coefficients than the latter during the initial sliding stage. As the sliding time increases, the heat

produced during wearing induces the local phase transformation from B19'/R to B2 in the surface layer in the former; thus impairing its superelasticity and resulting in larger friction coefficients. In sample B with a higher porosity, a high annealing temperature enhances the wear resistance as

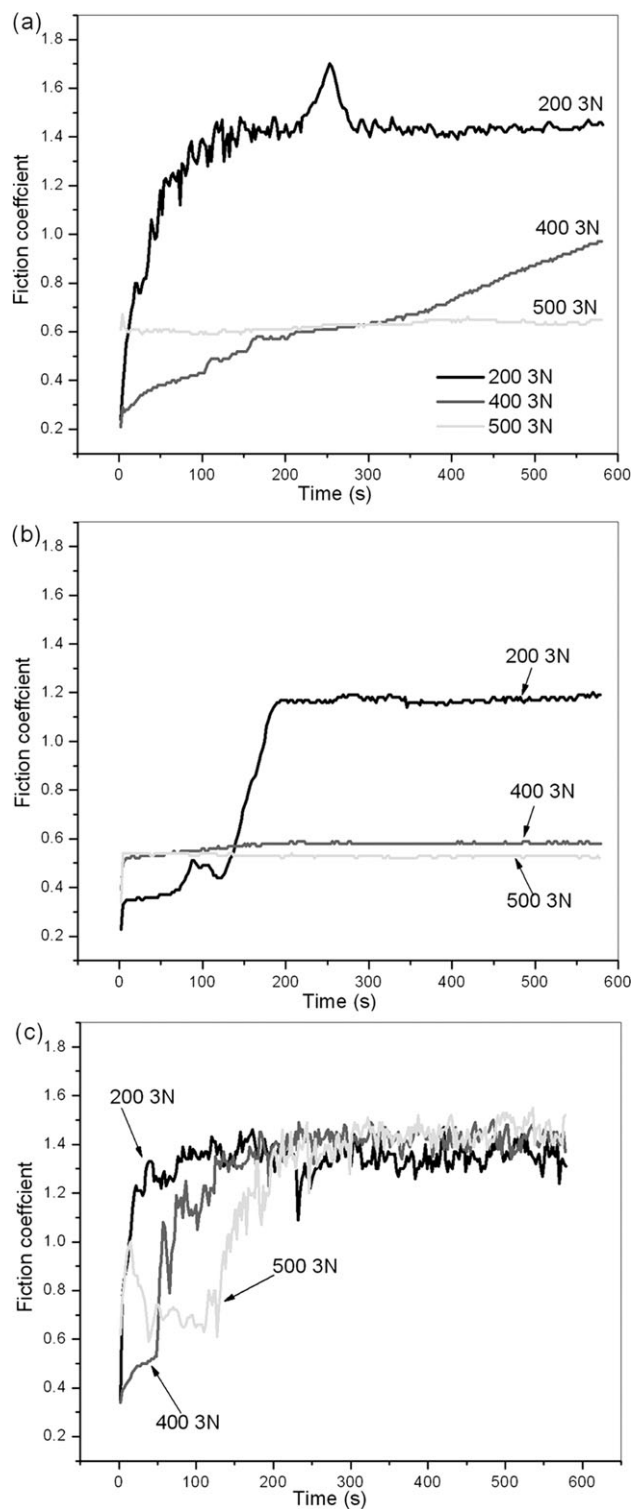


FIGURE 15. Evolution of friction coefficients of NiTi samples annealed at 200, 400, and 500°C: (a) A, (b) B, and (c) D.

shown in Figure 15(b). However, after annealing at 200°C and under a load of 3 N, the initial track from 0 to 130 s reveals the lowest friction coefficients. As aforementioned, although the surface oxide film improves the wear resistance of the dense NiTi in the initial stage, it cannot contribute to the tribological performance of porous NiTi, especially ones with high porosity, because of the broken surface structure. Hence, this phenomenon should be attributed to other factors. As shown in Figure 8(c), annealing at 200°C cannot activate the phase transformation in sample B, but according to the XRD peak intensity in Figure 2(b), the B19' phase is larger than B2. The stress in the surface layer produced by a bigger applied load can induce superelasticity during the wear test producing smaller friction coefficients. However, similar to the sample annealed at 400°C under a load of 3 N [Fig. 15(a)], the superelasticity in the surface layer is destroyed by heat under further sliding thereby increasing the friction coefficients. The same phenomenon can be observed from the same sample under a load of 2 N [Fig. 9(b)] but not so under 1 N [Fig. 9(a)]. It implies that an applied load of 1 N cannot activate the stress-induced superelasticity in the surface layer. As shown in Figure 15(c), it appears that the annealing temperature does not influence the tribological behavior of dense NiTi. In combination with the analysis of the phase transformation temperature shown in Figure 8(a), it can be concluded that the M_s temperature is not the dominant factor for the wear resistance of dense NiTi SMAs. It is in good agreement with reported results²⁵⁻³⁰ and the obvious difference is the extent of the region with low friction coefficients attributable to the surface oxide layer under different annealing temperature.

Wear morphologies. Figure 16 depicts the morphology of the wear tracks on the NiTi samples annealed at 200°C under a load of 3 N. For samples D and A, although we can observe the track clearly on the surface [shown in Fig. 16(a,e), respectively], it is obvious that the track of sample D is much wider and more apparent than the one of sample A. In addition, there is big wear debris on the former indicated by red arrows in Figure 16(a) while this phenomenon does not occur on the latter shown in Figure 16(f). The track of sample B is shown in Figure 16(g). It is very difficult to recognize the much blurry track between the two red arrows. The worn surface can be recognized clearly in the high magnification image in Figure 16(h), and the track is along the red arrow direction. These images reveals that sample B of 36 vol % porosity exhibits the highest wear resistance and dense NiTi sample D has the worst tribological performance. This result is in good accordance with the aforementioned tendency of friction coefficients shown in Figure 9(c) and that higher porosity can enhance the wear resistance of porous NiTi scaffolds. The wear tracks of 400°C annealed samples under a load of 3 N are shown in Figure 17. For sample D, the track is much wide and there exists debris shown in Figure 17(a), and the high magnification indicates that the debris includes lots of tiny ones and big one with many cracks [Fig. 17(b)]. In comparison with dense NiTi, as shown in Figure 17(d), porous sample A has

a dim and narrow track, and no apparent debris can be observed on it. As the porosity is increased to 36 vol %, any trail of wear cannot be found on the worn sample B examined by SEM shown in Figure 17(e). These wear morphologies also confirm our previous deduction from Figure 11(c). Figure 18 shows the wear morphologies of 500°C annealed samples under a load of 3 N. We ground the cross-section to observe the cross-section morphologies. Like 200°C and 400°C annealed sample D, there is also a wide track on the surface of 500°C annealed sample D, and lots of debris forms along the track shown in Figure 18(a). The magnified image shown in Figure 18(b) indicates that grooves forms on the track marked by blue arrow, and a thin loosening layer with small cracks can be observed on the top surface marked by red frame. There are apparent big split between debris and substrate indicated by red arrows. Because we cannot recognize the wear tracks of 500°C annealed samples A and B directly like 400°C annealed sample B, we applied a dip angle to samples before SEM examination. However, the wear circle of sample A is still indistinct marked by red arrow shown in Figure 18(c), and it can be recognized more clearly by OM [indicated by red arrow in Fig. 18(d)]. In comparison with sample A, this dim wear track cannot be observed by SEM on the surface of sample B [Fig. 18(e)], and it can only be distinguished through OM shown in Figure 18(f). It can be concluded that high porosity samples possess better wear resistance, which also supports the deduction by tribological coefficients in Figure 13(c).

Mechanisms. Aging of baby boomers and traumatic injuries are placing high demands on bone substitutes for bone repair and reconstruction. Among the various artificial hard tissue replacement materials, metallic implants made of titanium alloys, NiTi SMAs, and stainless steels are most widely used in orthopedic implants due to their good strength, ductility, and biocompatibility. However, wear debris released from all-metal implants can cause osteocyticosteolysis at the interface with bone tissues leading to potential implant failure. It has been proposed that the main wear mechanisms in dense metal-on-metal (MOM) systems are adhesion,²⁰ abrasion,^{20,48-50} delamination,⁵⁰ surface fatigue,⁵¹ and tribochemical reactions.^{48,52} One of the most important wear mechanisms for dense alloys is abrasion dominant in many practical situations, especially under high loads or on surface-modified metals. However, in the ball-on-porous metal system, there are two different opinions on the role of the pores. The first is the negative effects of the pores on wear resistance proposed by Ye et al. They have found that pores or voids in the NiTi-based composites are detrimental to the composite wear resistance. The voids may act as stress raisers to diminish the wear resistance of the composites and improved wear resistance can be anticipated by reducing the porosity by HIP.^{22,53} On the other hand, Salahinejad et al. reveal that the porous stainless steel can exhibit outstanding wear resistance compared with dense AISI 316L stainless steel. It results from the specific configuration of the pores in the substrate and its considerable intrinsic

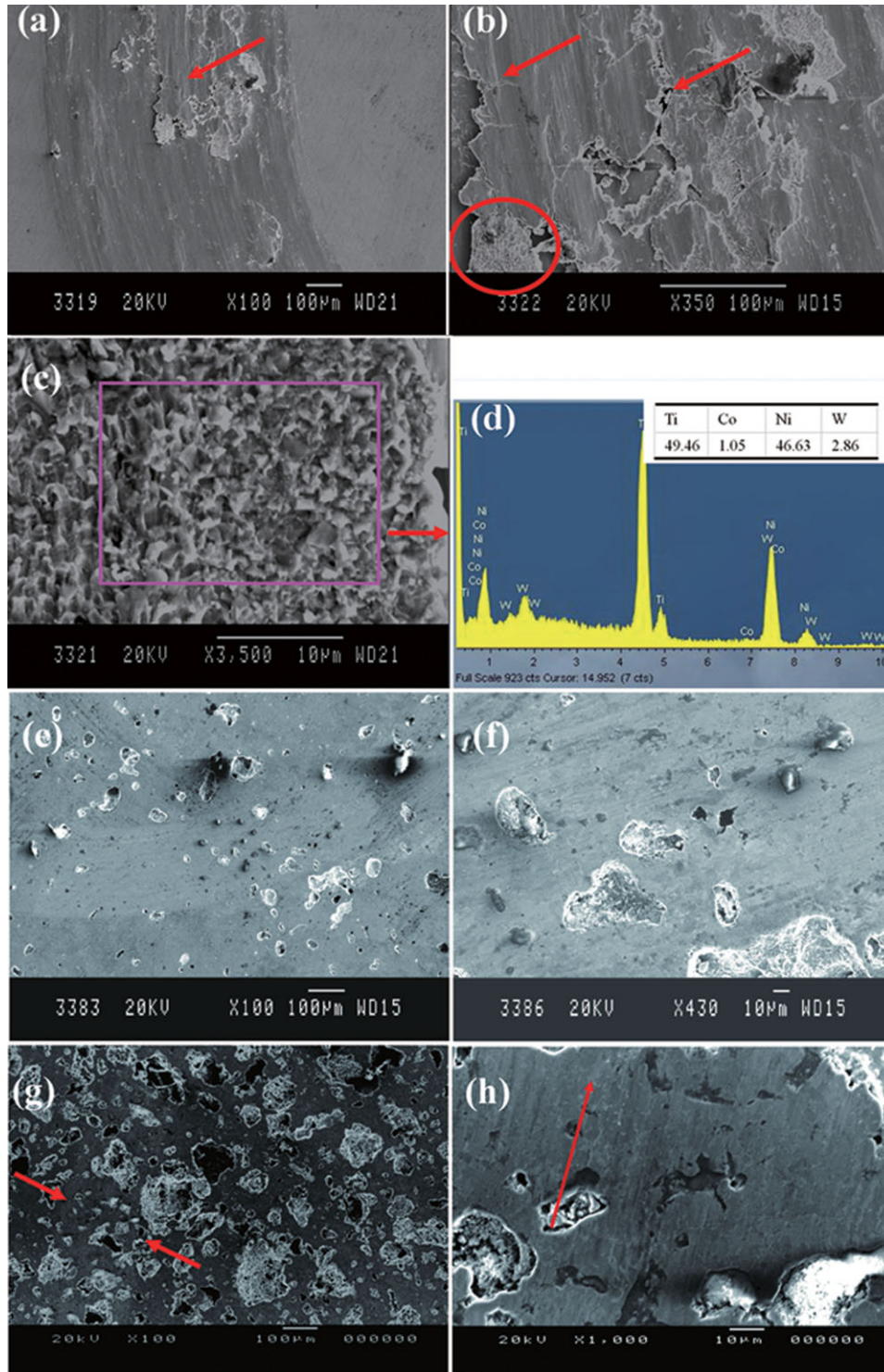


FIGURE 16. SEM images of track morphologies of 200°C annealed samples under 3 N. (a) D; (b) high magnification of (a); (c) high magnification of (b) indicated by red circle; (d) EDS pattern of (c); insert table shows atomic percentage; (e) A; (f) high magnification of (e); (g) B; (h) high magnification of (g). [Color figure can be viewed in the online issue, which is available at wileyonlinelibrary.com.]

hardness.⁵⁴ Our results are in good agreement with the latter as confirmed by the wear morphologies shown in Figures 16–18. In conventional porous alloys, this phenomenon can be explained by the following equation proposed by Tsui et al.⁵⁵:

$$P_y = 0.78r^2 \left(\frac{H^3}{E^2} \right) \quad (2)$$

where P_y is the resistance to plastic deformation, r is the radius of the rigid ball in contact with the alloy, H is the hardness, and E represents the elastic modulus. Our

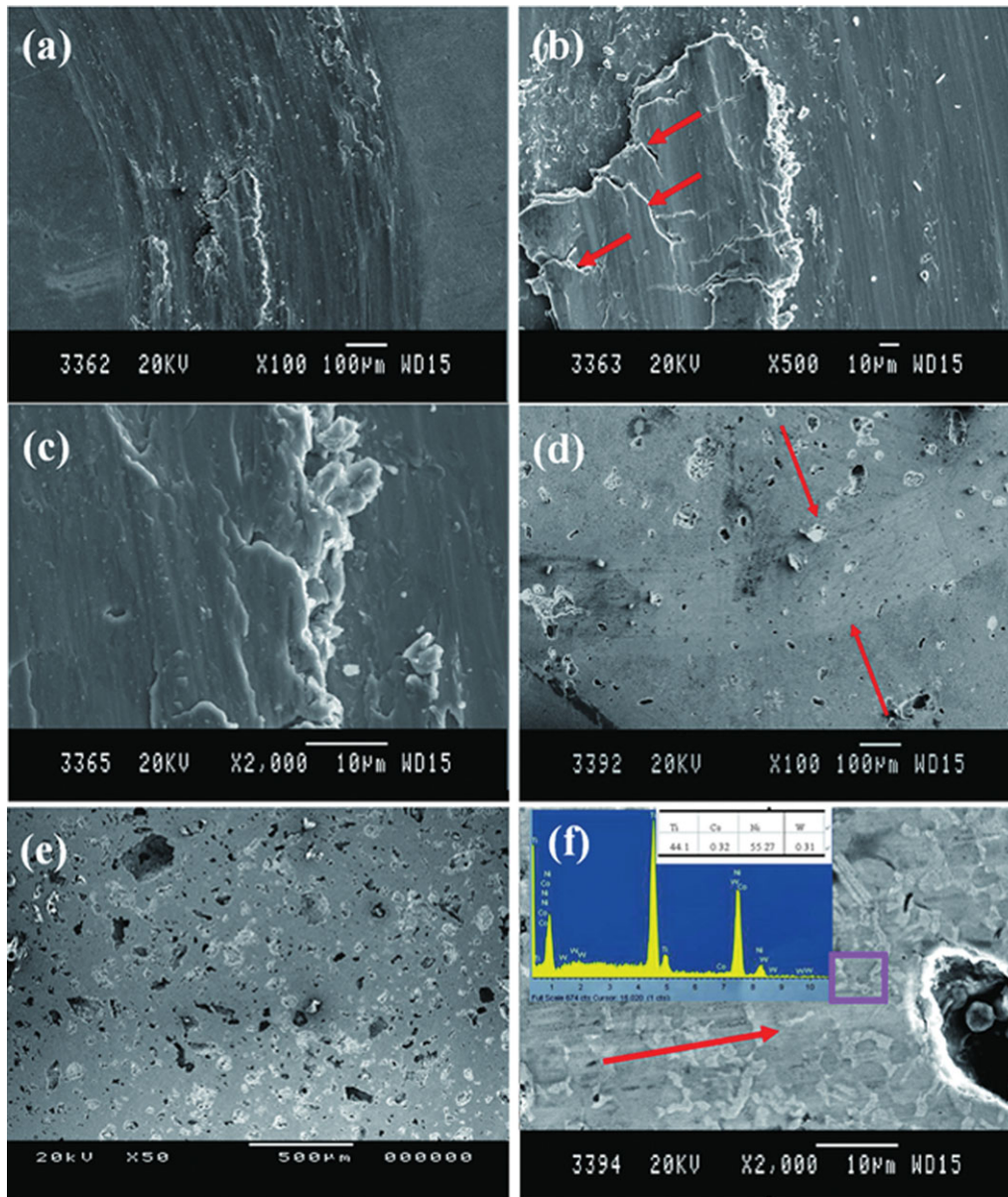


FIGURE 17. SEM images of track morphologies of 400°C annealed samples under 3 N. (a) D; (b) High magnification of (a); (c) high magnification of (b); (d) A; (e) B; (f) high magnification of (d); insert image and table are the EDS pattern and atomic percentage, respectively. [Color figure can be viewed in the online issue, which is available at wileyonlinelibrary.com.]

previous work confirms that porous structure can significantly reduce the high Young's modulus of 80 GPa of austenitic dense NiTi to 6–11 GPa of porous NiTi.⁵ As the porosity is increased, the Young's modulus is decreased.^{4,5} Generally, in the same phase and under the same environment, the hardness should be constant. However, as the measured value in Figures 10, 12, and 14 by nanoindenter, porous samples exhibit higher hardness than dense NiTi. One factor is the aforementioned partial phase transformation around indenter only for sample that has coexistence of soft phase B19'/R and hard B2. The other factor is the annealing–precipitation of minor second phases in porous NiTi alloys that strengthen substrates. Hence, in comparison with dense NiTi and according to Eq. (2), porous materials

can have higher P_y value, that is, enhanced resistance to plastic deformation. On the basis of Griffith's crack propagation theory, Leyland and Matthews have developed an interfacial fracture toughness theory. The fracture toughness of the MOM system during wear can be expressed by the following equation⁵⁶:

$$G_c = \sigma_c^2 \frac{\pi a}{E} \quad (3)$$

where a is the critical crack size and σ_c is a critical stress for the fast fracture that is related to P_y . Therefore, the higher fracture toughness value G_c of the alloy is determined by the larger hardness H and smaller elastic modulus E during the tribological tests. Hence, it can be deduced

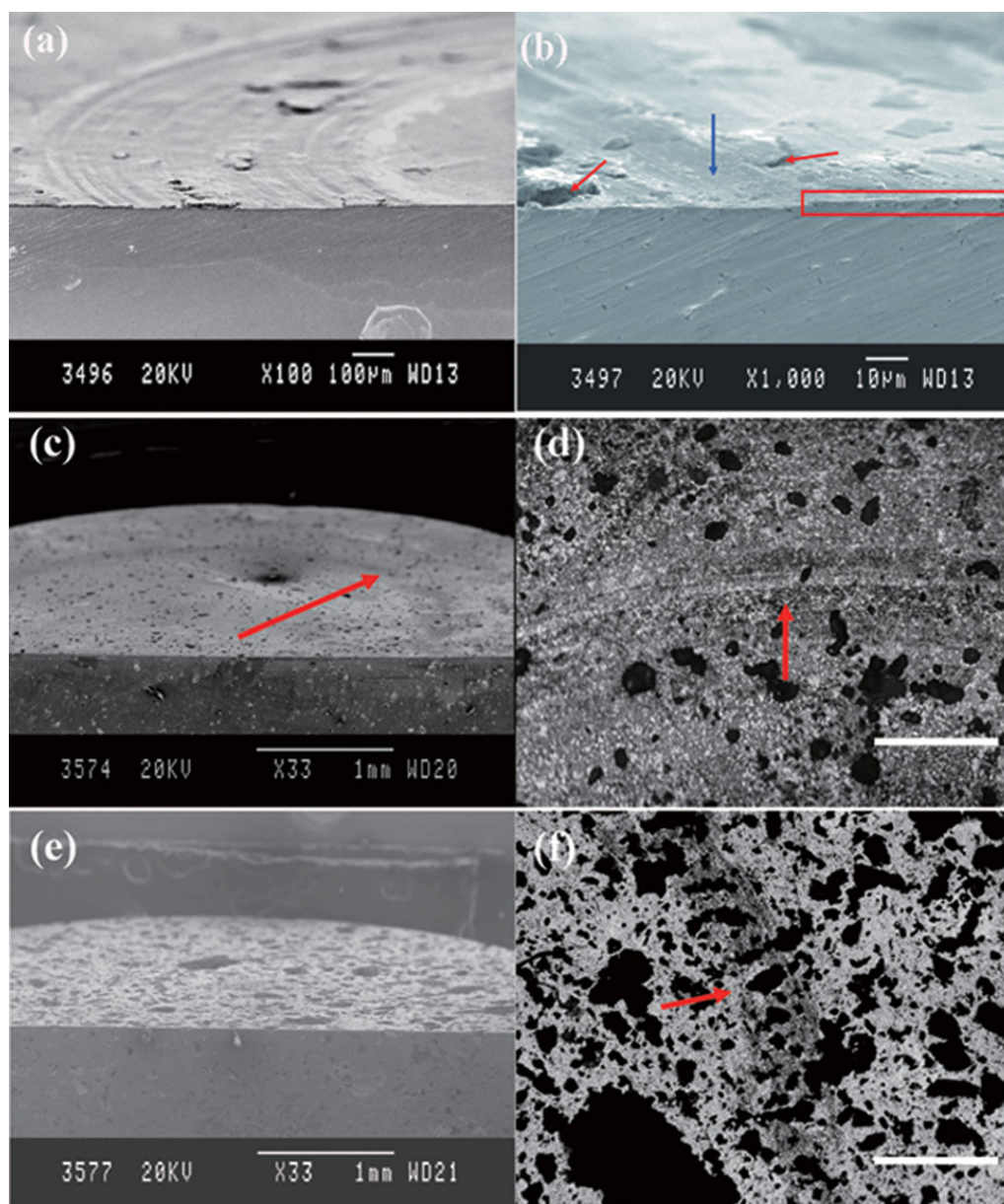


FIGURE 18. SEM images of track morphologies of 500°C annealed samples under 3 N. (a) D; (b) high magnification of a; (c) A; (d) OM image of A, scale bar = 500 μm ; (e) B; (f) OM image of B, scale bar = 500 μm . [Color figure can be viewed in the online issue, which is available at wileyonlinelibrary.com.]

that the porous structure can improve the fracture toughness G_c and thus results in the enhanced interfacial wear resistance.

Figure 19 schematically illustrates the interfacial situation between WC-Co ball and NiTi alloys during sliding. In this work, as the above analyzed, dense NiTi D has lower P_y value. The wear process should be abrasion dominant sliding course, and thus the shear stress F plays an important role for the propagation of crack.⁵⁷ As marked by red arrows in Figures 16(b), 17(b), and 18(b), there exists some shear faults on the track, and the shear stress induces the propagation of crack. The delamination occurs in this course. Figure 16(c) shows the high magnification image of delaminated layer marked by red circle in Figure 16(b),

which exhibits rubbly layer. EDS pattern reveals that minor W and Co from the sliding ball have transformed into the debris [shown in Fig. 16(d)]. After 400°C annealing, it can be clearly found from Figure 17(c) that the shear stress induces the delamination for dense NiTi. Because of the larger P_y value, in comparison with dense NiTi, there are no obvious delamination on the track for porous sample A and B, which can be observed by high magnified SEM images Figures 16(f,h) and 17(f). Although minor W and Co have transformed into the surface detected by EDS in the insert image of Figure 17(f), no wear debris is found on the track. In addition, the EDS pattern confirms the existence of Ni-rich second phases.

In addition to the porous structure, porous NiTi has the unique stress/thermal-induced superelasticity and complex

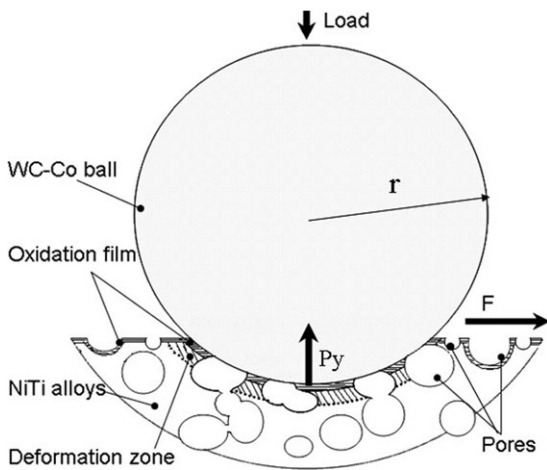


FIGURE 19. Schematic illustration of the ball-on-disk sliding process on the porous NiTi shape memory alloy.

phase transformation behavior under different temperature and they can influence the wear resistance appreciably. As aforementioned and in view of the broken oxide film shown in Figure 19, we can ignore the effects of natural oxidation on the wear resistance of porous NiTi, especially alloys with high porosity. A bigger load can induce a deformation zone in the near interfacial zone (depicted in Fig. 19). On the one hand, as deduced by Eq. (2), a given load can stimulate a bigger P_y in an alloy with larger porosity. The stress in the deformation zone reaches the critical value to more readily activate martensitic transformation and enhances the superelasticity and wear resistance of the NiTi with large porosity. On the other hand, Li has revealed that this stress-induced martensitic transformation diminishes the stress concentration in the deformation zone, especially at the tip of the microcracks, thus preventing the extension of cracks and consequently enhancing the wear resistance.²⁸ Peña et al.¹⁸ have revealed that in near equiatomic NiTi, the B2 phase possesses the largest hardness compared with the mixed phases (B2 + B19') and B19'. Therefore, according to Eqs. (2) and (3), the phase proportions in the porous NiTi alloys influence the wear resistance by altering the hardness as revealed by our results. For example, according to Figure 8(c), in NiTi with 36% porosity under RT, 400°C annealing yields more R phase, whereas annealing at 500°C gives rise to more B2 phase resulting in higher hardness and lower friction coefficients in the latter [Fig. 15(b)]. However, the situation becomes quite complex when both superelasticity and hardness (phase proportions) influence the tribological behavior. For instance, as shown in Figure 8(b), for NiTi with 18% porosity under a load of 3 N, 400°C annealing yields better superelasticity than 500°C annealing. The superelasticity plays a dominant role in the initially low friction coefficients compared with annealing at 500°C [Fig. 15(a)]. However, as heat generated from wearing can destroys the superelasticity by the interfacial phase transformation because the M_s is very close to RT [Fig. 8(b)], the hardness determines the tribological resistance gradually. Hence, the former shows higher friction coefficients than the latter.

CONCLUSIONS

The tribological properties of three-dimensional porous NiTi materials are studied systematically. Unlike dense NiTi, the surface oxide film has no obvious effects on the wear resistance of the porous alloys. Generally, a larger porosity yields better wear resistance and besides porosity, both the superelastic behavior, minor second phase and phase proportion in the porous NiTi affect the wear resistance of porous NiTi alloys. These factors are linked directly to the porosity and annealing temperature. Generally, a higher annealing temperature yields worse superelasticity and a large proportion of the higher hardness phase. The tribological performance of porous NiTi is dictated by the combined effects of porosity, superelasticity, and phases.

REFERENCES

- Helsen JA, Jurgen Breme H. *Metals as biomaterials*. New York: Wiley; 1998.
- Suchanek W, Yoshimura M. Processing and properties of hydroxyapatite-based biomaterials for use as hard tissue replacement implants. *J Mater Res* 1998;13:94–117.
- Itin VI, Gyunter VE, Shabalovskaya SA, Sachdeva RLC. Mechanical-properties and shape-memory of porous nitinol. *Mater Charact* 1994;32:179–187.
- Greiner C, Oppenheimer SM, Dunand DC. High strength, low stiffness, porous NiTi with superelastic properties. *Acta Biomater* 2005;1:705–716.
- Wu SL, Chung CY, Liu XM, Chu PK, Ho JPY, Chu CL, Chan YL, Yeung KWK, Lu WW, Cheung KMC, Luk KDK. Pore formation mechanism and characterization of porous NiTi shape memory alloys synthesized by capsule-free hot isostatic pressing. *Acta Mater* 2007;55:3437–3451.
- Neurohr AJ, Dunand DC. Shape-memory NiTi with two-dimensional networks of micro-channels. *Acta Biomater* 2011;7:1862–1872.
- Zhao Y, Taya M, Kang YS, Kawasaki A. Compression behavior of porous NiTi shape memory alloy. *Acta Mater* 2005;53:337–343.
- Liu XM, Wu SL, Yeung KWK, Chan YL, Hu T, Xu ZS, Liu XY, Chung CY, Cheung KMC, Chu PK. Relationship between osseointegration and super-elastic biomechanics in porous NiTi scaffolds. *Biomaterials* 2011;32:330–338.
- Assad M, Jarzem P, Leroux MA, Coillard C, Chernyshov AV, Charrette S, Rivard CH. Porous titanium–nickel for intervertebral fusion in a sheep model: Part 1. Histomorphometric and radiological analysis. *J Biomed Mater Res Part B* 2003;64:107–120.
- Wu SL, Liu X, Hu T, Chu PK, Ho JP, Chan YL, Yeung KWK, Chu CL, Hung TF, Huo KF, Chung CY, Lu WW, Cheung KMC, Luk KDK. A biomimetic hierarchical scaffold: Natural growth of nanotitanates on three-dimensional microporous Ti-based metals. *Nano Lett* 2008;8:3803–3808.
- Sargeant TD, Guler MO, Oppenheimer SM, Mata A, Satcher RL, Dunand DC, Stupp SI. Hybrid bone implants: Self-assembly of peptide amphiphile nanofibers within porous titanium. *Biomaterials* 2008;29:161–171.
- Wu SL, Liu X, Chan YL, Chu PK, Chung CY, Chu CL, Yeung KWK, Lu WW, Cheung KMC, Luk KDK. Nickel release behavior and surface characteristics of porous NiTi shape memory alloy modified by different chemical processes. *J Biomed Mater Res Part A* 2009; 89:483–489.
- Wu SL, Liu XM, Chan YL, Chung CY, Chu PK, Chu CL, Lam KO, Yeung KWK, Lu WW, Cheung KMC, Luk KDK. In vitro bioactivity and osteoblast response on chemically modified biomedical porous NiTi synthesized by capsule-free hot isostatic pressing. *Surf Coat Technol* 2008;202:2458–2462.
- Wu SL, Chu PK, Liu XM, Chung CY, Ho JPY, Chu CL, Tjong SC, Yeung KWK, Lu WW, Cheung KMC, Luk KDK. Surface characteristics, mechanical properties, and cytocompatibility of oxygen plasma-implanted porous nickel titanium shape memory alloy. *J Biomed Mater Res Part A* 2006;79:139–146.

15. Yuan B, Li H, Gao Y, Chung CY, Zhu M. Passivation and oxygen ion implantation double surface treatment on porous NiTi shape memory alloys and its Ni suppression performance. *Surf Coat Technol* 2009;204:58–63.
16. AMstutz HC, Campbell P, Kossovsky N, Clarke IC. Mechanism and clinical-significance of wear debris-induced osteolysis. *Clin Orthop Rel Res* 1992;276:7–18.
17. Lohmann CH, Schwartz Z, Köster G, Jahn U, Buchhorn GH, MacDougall MJ, Casasola D, Liu Y, Sylvia VL, Dean DD, Boyan BD. Phagocytosis of wear debris by osteoblasts affects differentiation and local factor production in a manner dependent on particle composition. *Biomaterials* 2000;21:551–561.
18. Peña J, Solano E, Mendoza A, Casals J, Planell JA, Gil FJ. Effect of the Ms transformation temperature on the wear behaviour of NiTi shape memory alloys for articular prosthesis. *Biomed Mater Eng* 2005;15:289–293.
19. Liu R, Li DY. Experimental studies on tribological properties of pseudoelastic TiNi alloy with comparison to stainless steel 304. *Metall Mater Trans A* 2000;31:2773–2783.
20. Liu XM, Wu SL, Chan YL, Chu PK, Chung CY, Chu CL, Yeung KWK, Lu WW, Cheung KMC, Luk KDK. Structure and wear properties of NiTi modified by nitrogen plasma immersion ion implantation. *Mater Sci Eng A* 2007;444:192–197.
21. Man HC, Zhang S, Cheng FT. Improving the wear resistance of AA 6061 by laser surface alloying with NiTi. *Mater Lett* 2007;61:4058–4061.
22. Ye HZ, Li DY, Eadie RL. Influences of porosity on mechanical and wear performance of pseudoelastic TiNi-matrix composites. *J Mater Eng Perform* 2001;10:178–185.
23. Abedini M, Ghasemi HM, Ahmadabadi MN. Tribological behavior of NiTi alloy against 52100 steel and WC at elevated temperatures. *Mater Charact* 2010;61:689–695.
24. Arciniegas M, Casals J, Manero JM, Pena J, Gil F. Study of hardness and wear behaviour of NiTi shape memory alloys. *J Alloy Compd* 2008;460:213–219.
25. Zhang C, Farhat ZN. Sliding wear of superelastic TiNi alloy. *Wear* 2009;267:394–400.
26. Lin HC, Liao HM, He JL, Lin KM, Chen KC. Wear characteristics of ion-nitrided Ti50Ni50 shape memory alloys. *Surf Coat Technol* 1997;92:178–189.
27. Jin JL, Wang HL. Wear resistance of TiNi alloys. *Acta Metall Sin* 1988;24:A66–A70.
28. Li DY. A new type of wear-resistant material: Pseudo-elastic TiNi alloy. *Wear* 1998;221:116–123.
29. Liang YN, Li SZ, Jin YB, Jin W, Li S. Wear behavior of a TiNi alloy. *Wear* 1996;198:236–241.
30. Yan WY. Theoretical investigation of wear-resistance mechanism of superelastic shape memory alloy NiTi. *Mater Sci Eng A* 2006;427:348–355.
31. Liu F, Xu JL, Yu DZ, Wang FP, Zhao LC. Wear resistance of micro-arc oxidation coatings on biomedical NiTi alloy. *J Alloy Compd* 2009;487:391–394.
32. Wu SL, Liu XM, Yeung KWK, Hu T, Xu ZS, Chung CY, Chu PK. Hydrogen release from titanium hydride in foaming of orthopedic NiTi scaffolds. *Acta Biomater* 2011;7:1387–1397.
33. Wu SL, Liu XM, Chung CY, Chu PK, Chan YL, Yeung KWK, Chu CL. Biomimetic deposition of apatite on surface chemically modified porous NiTi shape memory alloy. *Surf Rev Lett* 2008;15:97–104.
34. Liu XM, Wu SL, Chan YL, Chu PK, Chung CY, Chu CL, Yeung KWK, Lu WW, Cheung KM, Luk KDK. Surface characteristics, biocompatibility and mechanical properties of nickel-titanium plasma-implanted with nitrogen at different implantation voltages. *J Biomed Mater Res Part A* 2007;82:469–478.
35. Wu SL, Liu XM, Hu T, Jiang J, Chu PK, Yeung KWK, Chung CY, Chu CL, Xu ZS, Lu WW, Cheung KMC, Luk KDK. Electrochemical stability of orthopedic porous NiTi shape memory alloys treated by different surface modification techniques. *J Electrochem Soc* 2009;156:C187–C194.
36. Karageorgiou V, Kaplan D. Porosity of 3D biomaterial scaffolds and osteogenesis. *Biomaterials* 2005;26:5474–5491.
37. Itala AI, Ylanen HO, Ekholm C, Karlsson KH, Aro HT. Pore diameter of more than 100 μm is not requisite for bone ingrowth in rabbits. *J Biomed Mater Res* 2001;58:679–683.
38. Wu SL, Liu XM, Chu PK., Chung CY, Chu CL, Yeung KWK. Phase transformation behavior of porous NiTi alloys fabricated by capsule-free hot isostatic pressing. *J Alloy Compd* 2008;449:139–143.
39. Li BY, Rong LJ, Li YY, Gjunter VE. Synthesis of porous Ni-Ti shape memory alloys by self-propagating high-temperature synthesis: Reaction mechanism and anisotropy pore structure. *Acta Mater* 2000;48:3895–3904.
40. Chu CL, Chung CY, Lin PH, Wang SD. Fabrication of porous NiTi shape memory alloy for hard tissue implants by combustion synthesis. *Mater Sci Eng A* 2004;366:114–119.
41. Lagoudas DC, Vandygriff EL. Processing and characterization of NiTi porous SMA by elevated pressure sintering. *J Intel Mater Syst Struct* 2002;13:837–850.
42. Tang CY, Zhang LN, Wong CT, Chan KC, Yue TM. Fabrication and characteristics of porous NiTi shape memory alloy synthesized by microwave sintering. *Mater Sci Eng A* 2011;528:6006–6011.
43. Whitney M, Corbin SF, Gorbet RB. Investigation of the mechanisms enactive sintering and combustion synthesis of NiTi using differential scanning calorimetry and microstructural analysis. *Acta Mater* 2008;56:559–570.
44. Alloy Phase Diagrams Book, vol. 3. Materials Park, OH: ASM International; 1992.
45. Tan L, Crone WC. Surface characterization of NiTi modified by plasma source ion implantation. *Acta Mater* 2002;50:4449–4460.
46. La P, Xue Q, Liu W. Effects of boron doping on tribological properties of Ni3Al–Cr7C3 coatings under dry sliding. *Wear* 2001;249:93–99.
47. Guo C, Zhou JS, Zhao JR, Wang LQ, Yu YJ, Chen JM, Zhou HD. Microstructure and tribological properties of a HfB₂-containing Ni-based composite coating produced on a pure Ti substrate by laser cladding. *Tribol Lett* 2011;44:187–200.
48. Wimmer MA, Loos J, Nassutt R, Heitkemper M, Fischer A. The acting wear mechanism on metal-on-metal hip joint bearings: In vitro results. *Wear* 2001;250:129–139.
49. Sieber HP, Rieker CB, Kottig P. Analysis of 118 second-generation metal-on-metal retrieved hip implants. *J Bone Joint Surg Br* 1999;81:46–50.
50. Hu T, Wen CS, Sun GY, Wu SL, Chu CL, Wu ZW, Li GY, Lu J, Yeung KWK, Chu PK. Wear resistance of NiTi alloy after surface mechanical attrition treatment. *Surf Coat Technol* 2010;205:506–510.
51. Chiba A, Kumagai K, Nomura N, Miyakawa S. Pin-on-disk wear behavior in a like-on-like configuration in a biological environment of high carbon cast and low carbon forged Co–29Cr–6Mo alloys. *Acta Mater* 2007;55:1309–1318.
52. Wimmer MA, Sprecher C, Täger G, Fischer A. Tribochemical reaction on metal-on-metal hip joint bearings: A comparison between in-vitro and in-vivo results. *Wear* 2003;255:1007–1014.
53. Ye HZ, Li DY, Eadie RL. Improvement in wear resistance of TiNi-based composites by hot isostatic pressing. *Mater Sci Eng A* 2002;329–331:750–755.
54. Salahinejad E, Amini R, Marasi M, Hadianfard MJ. Microstructure and wear behavior of a porous nanocrystalline nickel-free austenitic stainless steel developed by powder metallurgy. *Mater Des* 2010;31:2259–2263.
55. Tsui TY, Pharr GM, Oliver WC, Bhatia CS, White RL, Anders S, Anders A, Brown IG. Nanoindentation and nanoscratching of hard carbon coatings for magnetic disks. *Mater Res Soc Symp Proc* 1995;383:447–452.
56. Leyland A, Matthews A. On the significance of the H/E ratio in wear control: A nanocomposite coating approach to optimized tribological behaviour. *Wear* 2000;246:1–11.
57. Lawn BR. Indentation of ceramics with spheres: A century after hertz. *J Am Ceram Soc* 1998;81:1977–1994.